Halide-mediated modification of magnetism and electronic structure of alpha Co(II) hydroxides. Synthesis, characterization and DFT+U simulations

Víctor Oestreicher[1,2,†], Diego Hunt[3,†], Ramón Torres-Cavanillas[2], Gonzalo Abellán[2], Damián A. Scherlis[1], Matías Jobbágy[1*]

[1]Departamento de Química Inorgánica, Analítica y Química Física/INQUIMAE, Facultad de Ciencias Exactas y Naturales, Universidad de Buenos Aires, Ciudad Universitaria, Pab. II, Buenos Aires (C1428EHA) Argentina

[2]Instituto de Ciencia Molecular (ICMol), Universidad de Valencia, Catedrático José Betrán 2, 46980, Paterna, Valencia, Spain

[3]Departamento de Física de la Materia Condensada, GIyA, CAC-CNEA. Instituto de Nanociencia y Nanotecnología, CNEA-CONICET, San Martin (B1650) Buenos Aires, Argentina

[†]These authors contributed equally to this work.

[*]jobbag@qi.fcen.uba.ar

Abstract

The present study introduces a comprehensive exploration in terms of physicochemical characterization and calculations based on Density Functional Theory with the Hubbard's correction (DFT+U) of the whole family of α-Co(II) hydroxihalides (F, Cl, Br, I). These samples were synthesized at room-temperature employing an one-pot approach based on the epoxide route. A thoroughly characterization (PXRD, XPS, TGA-MS, magnetic and conductivity measurements) corroborated by the simulation is presented analysing structural, magnetic and electronic aspects. Beyond the inherent tendency of intercalated anions to modify the interlayer distance, the nature of the incorporated halide has a marked effect on several aspects. This includes the modulation of Co^{Oh} to Co^{Td} ratio, as well as the inherent tendency towards dehydration and irreversible decomposition. While the magnetic behaviour is strongly correlated with the Co^{Td} amount reflected in the presence of a glassy behaviour with high magnetic disorder, the electrical properties depends deeper on the nature of the halide. The computed electronic structures suggest that the Co^{Td} molar fraction exerts a minor effect on the inherent conductivity of the phases. However, the band gap of the solid turns out to be significantly dependent on the nature of the incorporated halide, governed by ligand to metal charge transfer, which minimized the gap as the anionic radius becomes larger. Conductivity measurements of pressed-pellets confirms this trend. To the best of our knowledge, this is the first report on the magnetic and electrical properties of α-Co(II) hydroxihalides validated with in silico descriptions, opening the gate for the rational design of layered hydroxylated phases with tuneable electrical, optical and magnetic properties.

1 Introduction

Layered materials consist of bidimensional chemically bonded lattices, periodically assembled between each other along the perpendicular direction through dispersive and/or electrostatic forces to give rise to three-dimensional crystals.[1] Among them, layered metal hydroxides have recently revealed as chemically active nanostructures suited for membranes, ionic exchangers, catalysts, electrochemical cells, or information storage devices.[2–7] Co(II) based layered hydroxides in particular gained attention due to their marked functionality in energy applications[8] and their intriguing fundamental properties. [9–11] This cation can adopt several coordination environments, including octahedral, tetrahedral, square-pyramidal, trigonal-bipyramid, and squareplanar, giving rise to an extremely rich variety of structures.[12–14]
Layered basic salts known as α-Co(II) hydroxides can be found either as strictly inorganic basic salts [15] or in their hybrid forms.[16–18] This intriging phase contains a predominant fraction of octahedral Co(II) centers, hereafter denoted as Co^{Oh}, which display a brucitic hexagonal arrange.[19] Certain Co^{Oh} positions of each layer are vacant, and these sites are occupied by a pair of tetrahedral Co(II) centers, Co^{Td}, placed externally to the hydroxilated layer, and presenting an exchangeable coordination position, as found in the well-defined mineral parent structure of simonkolleite, $Zn_3^{Oh}Zn_2^{Td}(OH)_8Cl_2 \cdot yH_2O$ (see Figure 1).[20] In the case of chloride coordinated phases, alternative synthetic, kinetically controlled procedures allowed for the modulation of the Co^{Oh} to Co^{Td} ratio, giving birth to a family of Co-layered hydroxides obeying to the general formula $Co_{1-x}^{Oh}Co_x^{Td}(OH)_{2-x}Cl_x \cdot yH_2O$, with $0.26 \leq x \leq 0.5$, exhibiting a disordered distribution of Co^{Td} sites within the layers.[21] DFT+U based calculations suggest that this variable stoichiometry has a noticeable influence on the electronic and magnetic structures of the material, even in a wider composition range.[11]

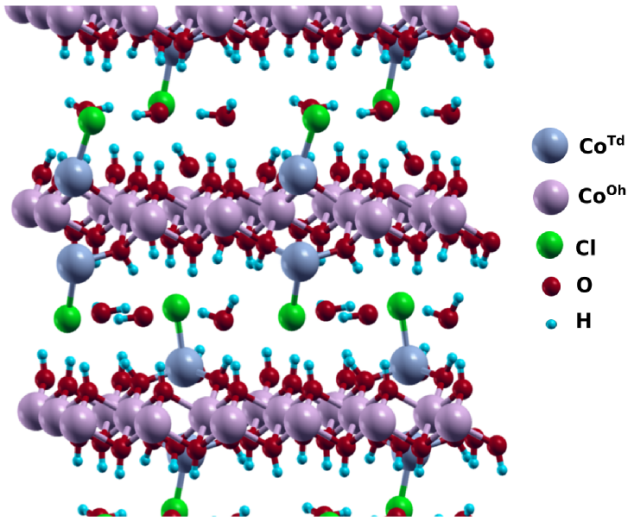

Figure 1: Schematic representation of the α-Co(II) lattice containing chloride. Both Co(II) environments are denoted: Co^{Oh} (pink) and Co^{Td} (blue); chloride ligands coordinated to Co^{Td} are also highlighted (green).

The preparation of pure α-Co(II) hydroxihalides constitutes a challenge for inorganic synthesis. Sasaki's team explored and optimized a hydrothermal route that, under a certain Co(II) to chloride concentration ratio, leads to the pure chloride from.[22] However, subsequent attempts to isolate other anions in Co(II) α-phases, based on the modification of this phase failed. Anionic exchange and recrystallization process resulted in the undesired segregation of β-$Co(OH)_2$ impurities. In recent years, the epoxide driven homogeneous alkalinization demonstrated to be a suitable approach to prepare a variety of layered double hydroxides[23–25], including the chloride form of the α-Co(II) and α-Ni(II) hydroxide[9]. In the present work, we revisited and optimized this synthetic method in order to prepare this α-Co(II) phase for the remnant halides (F, Br, I) in their corresponding highly cristalline forms, with the objective of comprehensively explore the structural, compositional and thermal stability features of these phases, which required the understanding of halide effect over the epoxide ring opening reaction. Electrical conductivity measurements, together with a macroscopic magnetic characterization, based on susceptibility and isothermal magnetization, were performed to understand the physical properties of theses phases. DFT+U calculations offer a complementary approach to the role of the halide ligand, highlighting its inherent role as modulator of the electronic and magnetic properties.

2 Materials and Methods

2.1 Chemicals

Cobalt nitrate hexahydrate ($Co(NO_3)_2 \cdot 6\,H_2O$), sodium fluoride (NaF), sodium chloride (NaCl), sodium bromide (NaBr), sodium iodide (NaI), sodium nitrate ($NaNO_3$) and glycidol (Gly) were purchased from Sigma-Aldrich and used without further purification. Ultrapure water was obtained from a Millipore Milli-Q® equipment.

2.2 Determination of alkalinization constants

Representative alkalinization kinetic runs were recorded d by *in situ* potentiometric pH measurement in glass reactor at 25 °C. Typically, alkalinization curves were carried out at a pH value of 3.0 ± 0.1 in HCl solution of Milli-Q® water containing NaX ($50 - 150$ mM), with X: NO_3^-, F^-, Cl^-, Br^- and I^-, and glycidol ([Gly] = $50 - 1000$ mM). Curves were analyzed as a function of the reduced time, t^*, defined as the time needed to reach a neutral pH, $t^* = t/t_{pH=7.0}$. Considering that $1/t_{pH=7.0}$ is proportional to the alkalinization rate, the corresponding constants for each halide were obtained as the slope of $1/t_{pH=7.0}$ as a function of halide and glycidol concentrations.[23]

2.3 Synthesis of α-X phases

All solids were prepared on the basis of an alternative one-pot epoxide route[9, 23] optimized on the basis of the inherent reactivity of the involved halides. Precipitations were driven from filtered solutions of Milli-Q® water containing cobalt nitrate, glycidol, and the corresponding

sodium halide, adjusted with HCl at an initial pH of 3.0 ± 0.1 and aged for 48 h at 25 °C under magnetic stirring. The initial condition to obtain the phases are reported in the Table 1. Representative alkalinization/precipitation curves were recorded by *in situ* potentiometric pH measurement in a reactor at 25 °C under permanent magnetic stirring. The precipitated products were collected by filtration, washed three times with Milli-Q® water, and dried at room temperature.

2.4 Characterization of the solid phases

All synthesized solids were characterized by powder X-ray diffraction (PXRD) using graphite-filtered Cu K_α radiation (λ =1.5406 Å) and a field emission scanning electron microscopy (FESEM) instrument, equipped with an energy dispersive X-ray spectroscopy (EDS) probe. X-ray Photoelectron Spectroscopy (XPS) was performed *ex situ* at the X-ray Spectroscopy Service at the Universidad de Alicante using a K_α X-ray photoelectron spectrometer system (Thermo Scientific). All spectra were collected using Al K_α radiation (1486.6 eV), monochromatized by a twin crystal monochromator, yielding a focused X-ray spot (elliptical in shape with a major axis length of 400 μm) at 3 mA.C and 12 kV. The alpha hemispherical analyzer was operated in the constant energy mode with survey scan pass energies of 200 eV to measure the whole energy band and 50 eV in a narrow scan to selectively measure the particular elements. XPS data were analyzed with Avantage software. UV-vis absorption spectra were recorded over the solid samples in a reflectance mode using an Ocean Optics spectrometer. Thermogravimetric analysis coupled with mass spectroscopy (TGA-MS) were carried out in a TA SDT Q600 instrument under air flow (100 $cm^3.min^{-1}$) at both 1 °C/min (without MS coupled) and 10 °C/min (with MS coupled).
Magnetic data were collected over the bulk material with a Quantum Design Superconducting Quantum Interference Device (SQUID) MPMS-XL-5. The magnetic susceptibility of the samples was corrected from the diamagnetic contributions of their atomic constituents as deduced from Pascals constant tables and the sample holder. The DC data were obtained under an external applied field of 100 or 1000 Oe in the $2 - 300$ K temperature range. Magnetization studies were performed between -5 and $+5$ T at a constant temperature of 2 K. The AC data were collected under an applied field of 3.95 Oe at 997, 110, 10 and 1 Hz.
Transport measurements have been performed over disc-shaped pressed pellets under pressure of *ca.* 0.05 MPa. of the different α-**X** samples by a two contact probes configuration through silver paste and platinum wires, in a temperature range of 300 to 400 K under a high vacuum in a Physical Properties Measurement System (Quantum Design PPMS-9). Electrical measurements have been performed in the PPMS chamber using a Keithley 6517b electrometer. Conductivity values were calculated by the application of $\sigma = (G.L)/(T.W)$, where G is the measured conductance, L the distance between electrodes, W the length of the electrodes and T the thickness of the pellets (Table S7). Activation energies were calculated by fitting a linear curve of the Arrhenius plot of the logarithm of the conductivity versus the inverse of the temperature in the range of $365 - 400$ K.

2.5 DFT calculations

All calculations were performed employing DFT as implemented in the Quantum Espresso code[26], which is based on the pseudopotential approximation to represent the ion-electron interactions, and plane waves basis sets to expand the Kohn-Sham orbitals. Ultrasoft type pseudopotentials were adopted, in combination with the Perdew, Burke, and Ernzerhof (PBE) formalism to compute the exchange-correlation term[27]. According to previous optimizations of related phases, the Hubbard parameter in the DFT+U calculations was fixed to 4.5 eV.[10, 11, 28–32] An energy threshold of 10^{-8} *au* was used for self-consistency, while for geometry optimizations the convergence criteria were 10^{-6} *au* for the energy and of 10^{-3} *au* for the forces per atom. To improve the numerical convergence a first-order Methfessel-Paxton spreading was implemented. The dispersive interactions were considered by including the DFT-D semiempirical correction originally introduced by Grimme[33] and implemented in a plane-waves framework by Barone and co-workers.[34] Non colinear calculations with spin-orbit contributions[35] were performed to assess the spin orientation of cobalt ions. In our previous study, we found an angle θ=60° for the magnetic moment of the metal ions with respect to the z axis.[11] Thus, unless indicated explicitly, all calculations presented henceforth have been performed with this value of θ. Consistently with our previous work,[11] the simulations were carried out on supercells with general formula $[\mathrm{Co_n^{Oh}Co_2^{Td}(OH)_{2n+2}X_2}]_\mathrm{m} \cdot (\mathrm{H_2O})_\mathrm{y.m}$, where n = 3, 8 and 15, m represents the number of layers, y the number of water molecules per layer, and X the type of halide anion. In the following, the aforementioned supercells will be referred to as $[\mathrm{Co_3^{Oh}Co_2^{Td}(OH)_8X_2}]$, $[\mathrm{Co_8^{Oh}Co_2^{Td}(OH)_{18}X_2}]$ and $[\mathrm{Co_{15}^{Oh}Co_2^{Td}(OH)_{32}X_2}]$, where the fraction of tetrahedral sites (x as expressed in the general formula given in the Introduction) is 0.4, 0.2, and 0.12 respectively [11]. These values of n and y are in line with the chemical compositions observed herein as well as the values reported by other researchers.[18, 19, 36] Supercells containing two layers were used to evaluate the influence of interlaminar water molecules.

3 Results and Discussion

The epoxide route for homogeneous alkalinization was extensively explored in the past employing chloride as the ring opening nucleophilic agent at 25 °C.[23] In that context, the reaction rate law and the inherent rate were parametrized, typically for glycidol. However, in the present case the preparation of the phases containing other halides required a reformulation of the synthesis conditions, in order to ensure quantitative precipitation in a suitable rate for crystallization. As a first step, the alkalinization rate in the presence of each one of the halides was assessed under different conditions (see Figure S1). Taking the reaction with chloride as a reference, the bromide and iodide driven processes were 4.5 and 24-fold faster, respectively (see Table S1). This tendency, observed varying halide and glycidol concentrations in the range 50-150 mM, obeys to the inherent nucleophilicity (polarizability) of these anions, well represented by their volume. This trend, in agreement with the one previously observed in non-aqueous and aqueous based related systems,[37] is shown in Figure S2. In these conditions, the reactivity of fluoride is extremely low; extrapolation of the observed trend suggests an inherent rate at least 10 times lower than the one corresponding to chloride. In addition to halides, nitrate was also examined, to find a negligible reactivity that points to the nitrate salt as a suitable source of Co(II) cation (see Figure S1).

As it was reported in a previous work[23], the epoxide route alkalinization rate depends on both chloride and epoxide concentration ($v_{[OH]} = k[Cl^-][Gly]$), while precipitation and alkalinization rates are strictly proportional. Hence, the present data on kinetic ring-opening constants allows to propose a synthetic scenario where alkalinization rate, and consequently precipitation rate, remain constant when these halides are employed. To this aim, the inherent faster rate of bromide and iodide was compensated with a lower initial concentration of glycidol. Due to the negligible reactivity of fluoride, NaCl ought to be added to ensure proper alkalinization and quantitative precipitation (see Table 1). The pH evolution recorded for each phase along the precipitation process is presented in Figure 2. Upon a moderate nucleation overshooting, all solids precipitated around a defined plateau value. The observed constancy of pH is indicative of a quasi-equilibrium situation governed by the solubility product of the growing phase.[23]

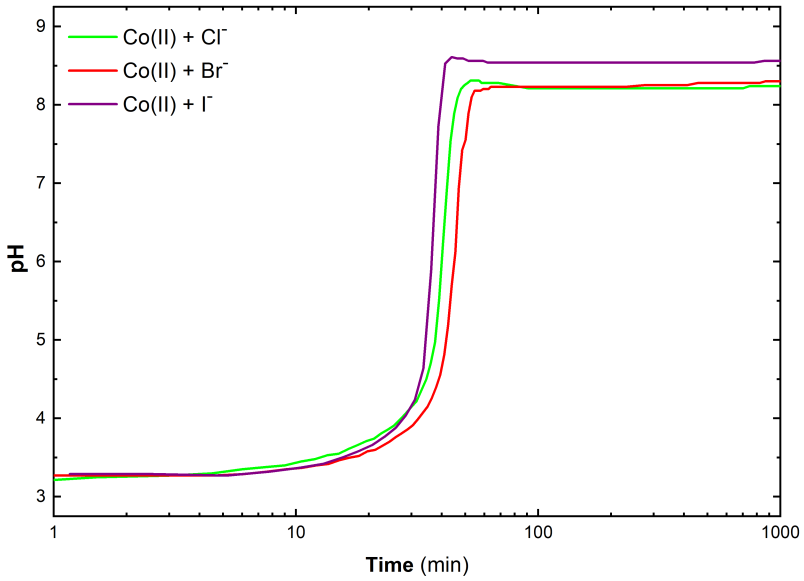

Figure 2: Precipitation curve at 25 °C for the different samples. α-Cl: NaCl: 50 mM; $Co(NO_3)_2$: 10 mM; Gly: 600 mM. α-Br: NaBr: 50 mM; $Co(NO_3)_2$: 10 mM; Gly: 133 mM. α-I: NaI: 50 mM; $Co(NO_3)_2$: 10 mM; Gly: 25 mM. All experiments were carried out at 25 °C and magnetic stirring.

The collected solid samples presented different colours. Whereas α-F was pink, the rest of the phases α-Cl, α-Br and α-I turned out to be markedly green, in agreement with previous reports[19, 21]. FESEM inspection of the solid samples confirmed the occurrence of single crystalline hexagonal platelets of 1-3 μm, exclusively, with a variable degree of coalescence or twinning (see Figure 3). EDS probe as well as XPS analysis confirmed the inclusion of the desired halide, exclusively; no traces of chloride were observed in the case of α-F. For all samples, the absence of nitrate was confirmed through FTIR spectroscopy (data not shown).

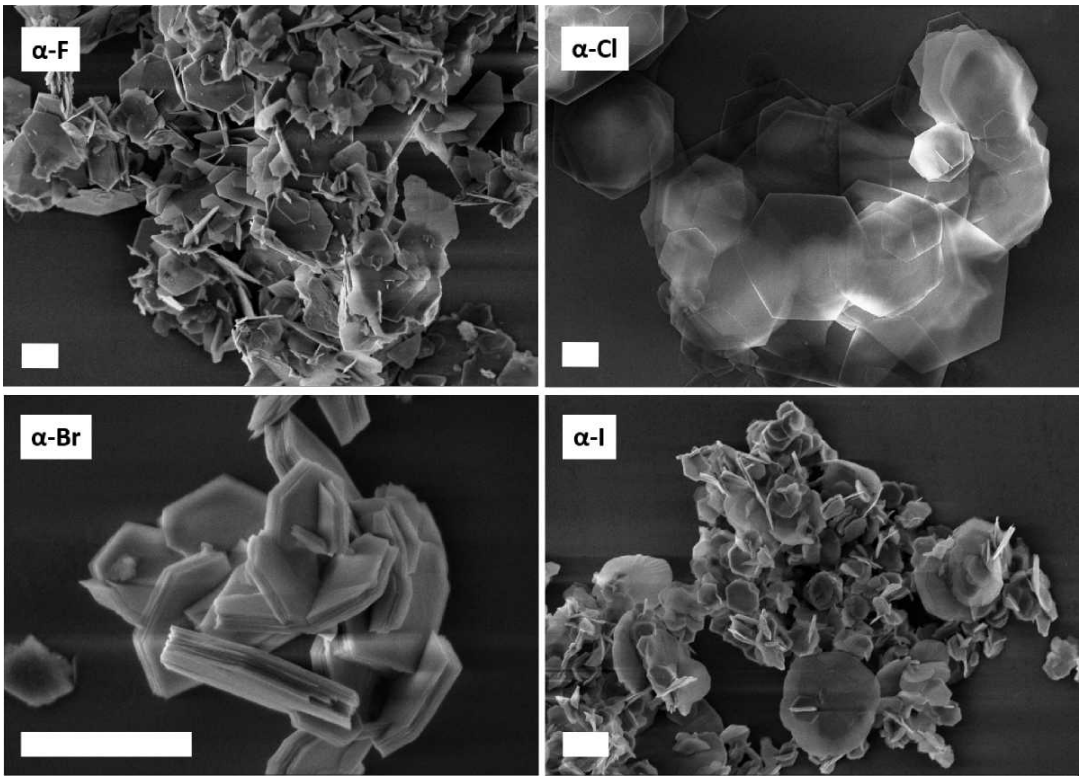

Figure 3: FESEM images for the synthesized α-X phases. The scale bars represent 1 μm.

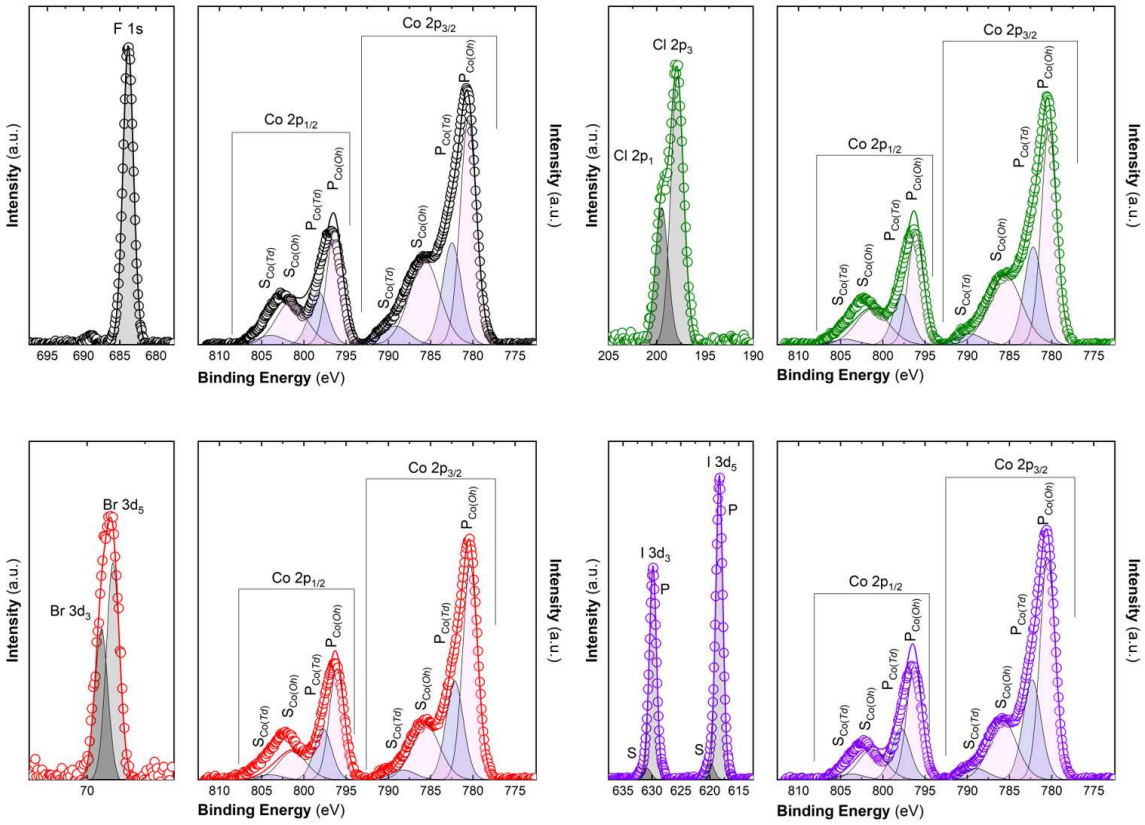

Figure 4: X-ray photoelectron spectra of α-X phases: α-F (black), α-Cl (green), α-Br (red) and α-I (purple). In all the cases for Co 2p core levels are presented as a decomposition of each band ($2\,p_{3/2}$ and $2\,p_{1/2}$) denoting two distinct cobalt species: Co(II) in octahedral (pink) and tetrahedral (blue). Both consisting of parent (P) and satellite (S) peaks from each species.

UV-Vis diffuse reflectance was recorded for all samples and a β-$Co(OH)_2$ reference phase (see Figure S3); in addition to the $465 - 530$ nm signal characteristic of Co^{Oh} centers, the spectra present an absorption band around 650 nm ascribable to ν_3(Td) transitions associated with the Co^{Td} centers [19, 21, 38]. Even in the case of α-F an absorption band around 650 nm is observed, confirming the presence of Co^{Td}. Figure 4 depicts the XPS spectra measured over the samples. In all the cases, XPS suggest an unequivocal environment for the halides.[21] However, in the case of cobalt, XPS confirms the presence of two crystallographic sites for Co(II): octahedral and tetrahedral, in concordance with UV-Vis diffuse reflectance.[21] Atomic percentages calculated by XPS allow to estimate the X : Co ratio, which is in good agreement with values obtained from EDS. Meanwhile, the ratio of Co^{Td} and X are close to one. Chemical composition estimated by XPS, EDS and TGA analysis of the obtained phases are compiled in Table 1.

A PXRD analysis of the obtained phases is presented in Figure 5. The characteristic reflections of α-Co(II)$-$Cl hydroxide previously reported for the hydrothermally crystallized chloride form can be seen in all the samples.[19] A continuous expansion in the interlamellar direction is

α-**X**	$[Co(NO_3)_2]$	[NaX] mM	[Gly]	Chemical composition
α-F	10	250(+50 NaCl)	600	$Co^{Oh}_{0.67}Co^{Td}_{0.33}(OH)_{1.67}F_{0.33} \cdot (H_2O)_{0.10}$
α-Cl	10	50	600	$Co^{Oh}_{0.74}Co^{Td}_{0.26}(OH)_{1.74}Cl_{0.26} \cdot (H_2O)_{0.33}$
α-Br	10	50	133	$Co^{Oh}_{0.86}Co^{Td}_{0.14}(OH)_{1.86}Br_{0.14} \cdot (H_2O)_{0.35}$
α-I	10	50	25	$Co^{Oh}_{0.88}Co^{Td}_{0.12}(OH)_{1.88}I_{0.12} \cdot (H_2O)_{0.50}$

Table 1: Experimental conditions for the synthesis and chemical composition of obtained α-X estimated by means of combined EDS, XPS and TGA analysis.

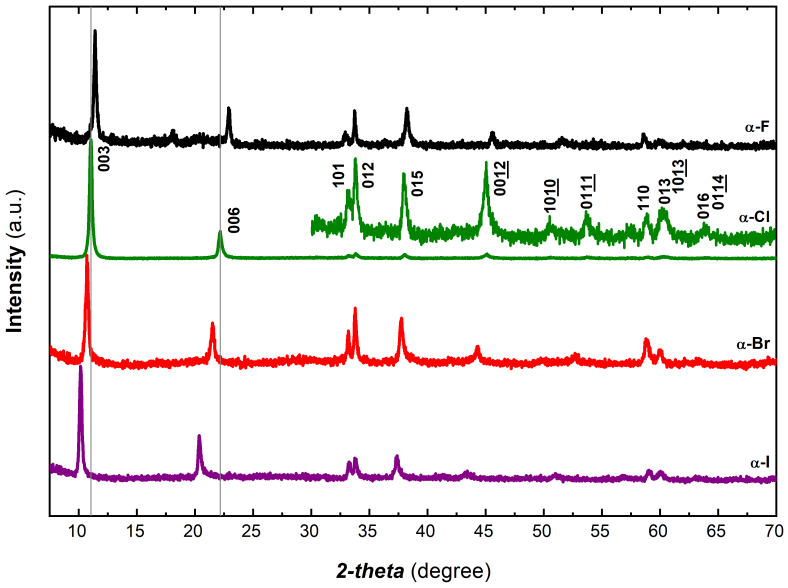

Figure 5: PXRD patterns recorded for the synthesized α-X phases. α-X phase is indexed according to Ref.[15].

observed for increasing halide's size. Main reflection related to interlamellar distance, indexed as (003), displaces from 11.93° to 10.15° from flouride to iodide, meanwhile in the case of (006) reflection shifts from 22.91° to 20.35°, respectively.
The structural characterization of these α-hydroxihalides, including the interlamelar (d_{003}) and intralamelar (d_{110}) distances are presented in Figure 6 as functions of the anionic diameter. While d_{110} remains almost invariant, a clear expansion is observed in the d_{003} distance as the size of the halide increases. Linear trends are observed for Cl, Br and I. Nevertheless, in the case of α-F the interlamelar distance turns out to be higher than expected. This result could be understood considering that the d_{003} distance is constrained by the presence of Co^{Td} in the interlamelar space (see Figure 1). The structural description provided by the DFT+U simulations is in good agreement with the structural parameters obtained from PXRD (see Figure 6). In addition, simulations were carried out with and without molecules of water in the interlamellar space. An expansion of around 4% in the d_{003} distance is observed in all

the cases, beyond the changes in composition, $\%Co^{Td}$ and X, or the number of intercalated molecules. Moreover, simulations suggest a negligible change in d_{110} (less than 0.05%).

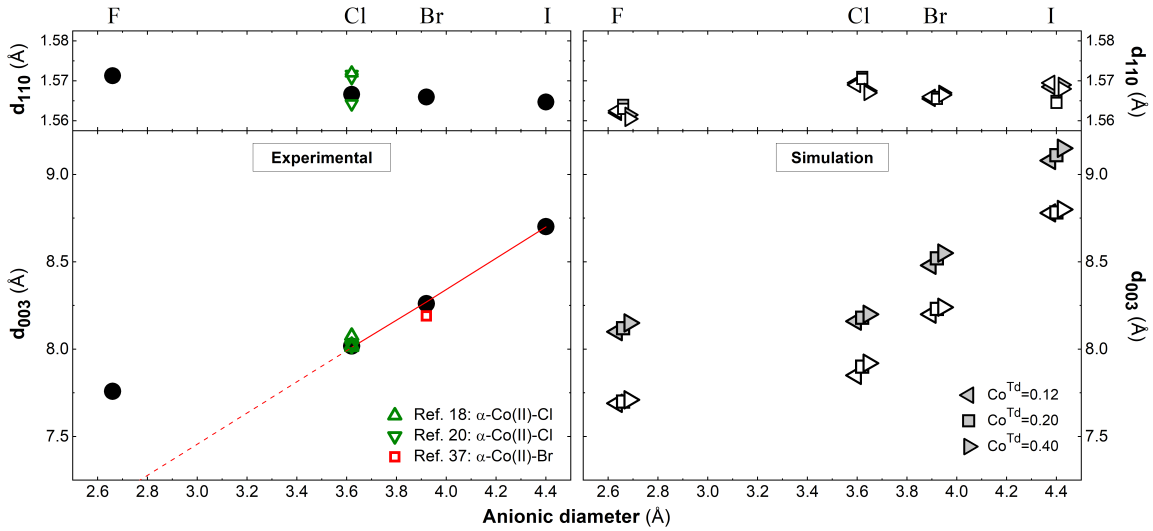

Figure 6: Experimental (left) and simulated (right) interlamelar (d_{003}) and intralamelar (d_{110}) distances for the α-X phases as functions of the anionic diameter of the included halide. Simulated distances are presented for hydrated (filled symbols) and dehydrated (empty symbols) phases in cells holding increasing amounts of Co^{Td}. Literature results for α-Co(II)$-$Cl[19, 21] and α-Co(II)$-$Br[39] are also presented. The number of water molecules included in $Co^{Td} = 0.12$, $Co^{Td} = 0.20$ and $Co^{Td} = 0.40$ supercells were 2, 3 and 5, respectively.

The DFT+U optimized interatomic distances between heavy atoms as a function of the anionic diameter are shown in Figure 7 for the different structures with representative fractions of tetrahedral sites. Whereas the $Co^{Td}-OH$ and $Co^{Oh}-OH$ distances remain practically invariant, obeying the characteristic distances found in the brucitic layer, the $Co^{Td}-X$ bond length becomes larger with the size of the halide, being the main factor responsible for the variation of d_{003}, and virtually the unique change in the structure.

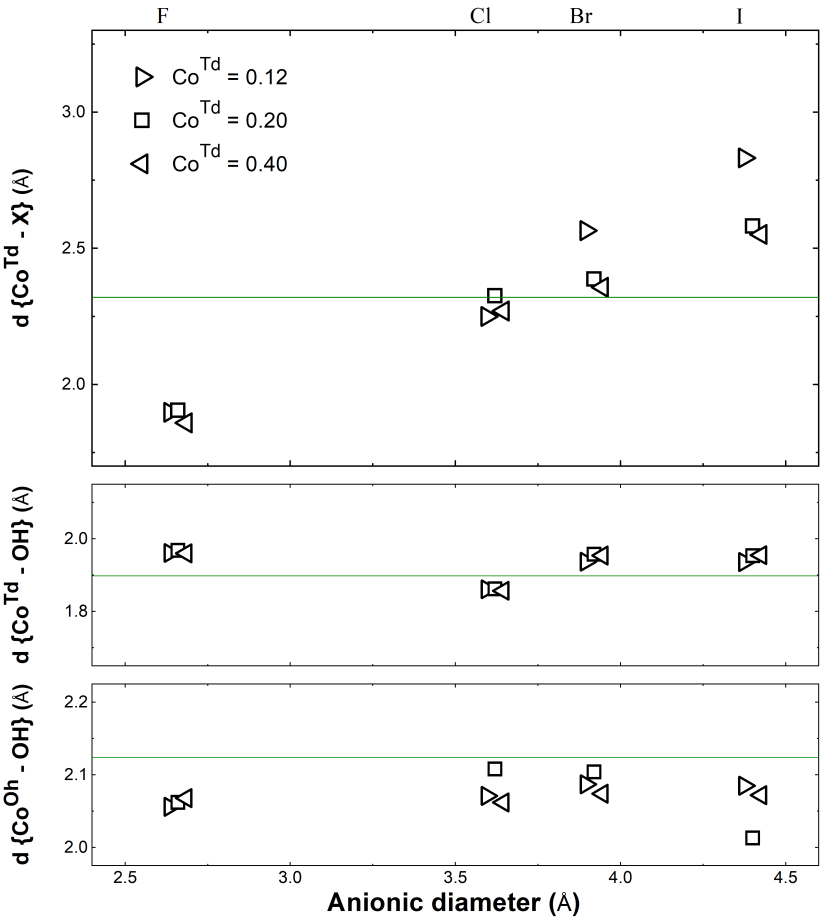

Figure 7: DFT+U optimized interatomic distances for α-X with different percentages of Co^{Td} as a function of the anionic diameter of the intercalated halides. The green line represents experimental values for the α-Co(II)−Cl phase reported in reference [19].

In order to obtain further information about the thermal stability and the decomposition regime of these phases, thermogravimetric analysis coupled with a mass spectroscopy (TGA-MS) was performed (see Figure 8), for the first time, to the best of our knowledge. Analysis was performed under oxidizing atmosphere at a heating rate of 10 °C/min, up to a final temperature of 700 °C. For all samples, the PXRD patterns of the remnant solids confirmed that this condition results in the quantitative decomposition of the hydroxides into the Co_3O_4 spinel (data not shown). In addition, no presence of halides were found in the resulting oxide by EDS. For each sample, a first mass loss step is observed below 150 °C. MS probe allows to assign this event to the loss of physisorbed and interlayer water molecules. The highest the halide's size, the lowest the dehydration temperature. For all samples, subsequent heating beyond 150 °C results in massive oxidative decomposition, in which the dehydration of structural OH groups coexists in part with the halide departure, either in the form of volatile acid, HX, or oxidized X_2. All the runs were repeated at 1 °C/min under similar atmosphere in order to ensure the separation of the consecutive dehydration and decomposition steps (see Figure S4). Figure S5 presents the dependence of Co^{Td} fraction and the dehydration temperature with the anionic

diameter. The higher the size of the halide, the lowest the Co^{Td} fraction and the lowest dehydration temperature. Similar results were reported for sulphate and acetate[40] and alkyl sulfates[12].

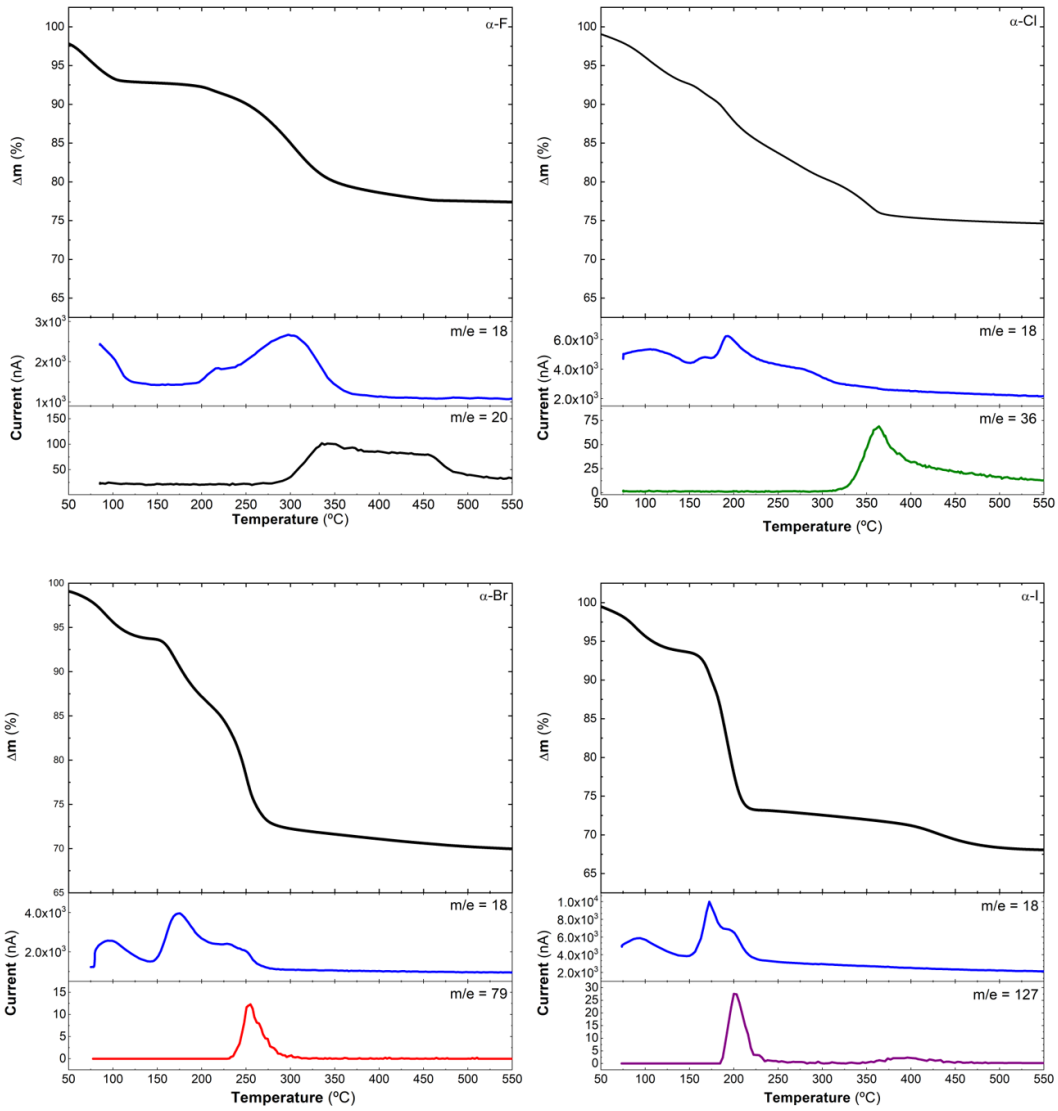

Figure 8: TGA-MS traces for α-F (upper left panel), α-Cl (upper right panel), α-Br (bottom left panel) and α-I (bottom right panel), decomposed in oxidizing atmosphere (80% N_2 and 20% O_2) at a heating rate of 10 °C/min.

Keeping in mind the thermal behaviour of α-X phases, simulations were carried out in order to understand the influence of water molecules in the interlayer space. Depending on the ambient humidity, the interlayer space can accommodate a variable number of water molecules.[41] This structural response to hydration, both in interlayer expansion and water configuration, is similar to that observed in related families of layered materials such as LDH.[42, 43] Figure 9 presents the hydration energy of the solid for different X and representatives n values, as a function of the number of water molecules in the interlayer space. The energy plotted in the figure, ΔE_{ads}, corresponds to the following process:

$$[Co_n^{Oh}Co_2^{Td}(OH)_{2n+2}X_2]_2 + yH_2O \longrightarrow [Co_n^{Oh}Co_2^{Td}(OH)_{2n+2}X_2]_2 \cdot (H_2O)_y$$

where the different α-X phases were simulated employing n=15 for all supercells.

The incorporation of water molecules into the interlayer space produces a strong stabilization

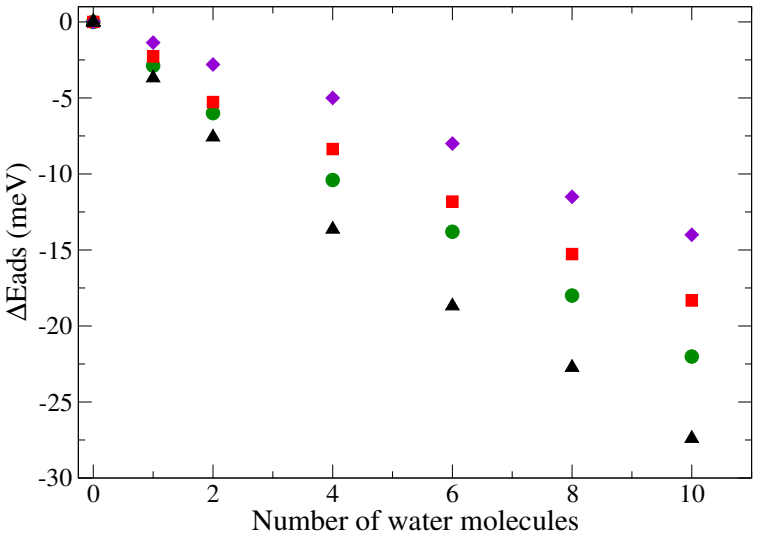

Figure 9: Computed hydration energies for $[Co_{15}^{Oh}Co_2^{Td}(OH)_{32}X_2]_2$ supercells as a function of the number of water molecules with X: α-F (black), α-Cl (green), α-Br (red) and α-I (purple).

of the structure with respect to their dehydrated phases. In the present case, simulation suggests a strong localization of water molecules close to the halide, mediated by hydrogen bonding (see Figure S6). These results are in contrast with the computational simulation carried out in LDH phases where water molecules mainly interact with OH sites.[44] Linear fit of the values represented in Figure 9 allowed for the estimation of water adsorption molar energy for each phase (see Figure S7 and Table S2). The trend on ΔE_{ads} is consistent with the trend on values of dehydration temperature determined by TGA (see Figures 8 and S4).

The potential energy surface associated with the hydrated crystal is very complex. Hence, the DFT+U optimized structures correspond to local minima and therefore the values reported should not be considered quantitatively but only as indicative of the trends. In order to achieve

a comprehensive role of confinement water in this sort of compounds, further simulations based on molecular dynamics are required.

Once the samples were chemically and structurally explored, a magnetic characterization was performed. Concerning to the magnetic behaviour of Co(II) layer hydroxides, β-$Co(OH)_2$ phase represents the simplest case of study, in which the metal ions adopts a common and univocal octahedral coordination. The overall magnetism in this phase is controlled by two main contributions: intralayer ferromagnetic (F) coupling between the octahedral centres through superexchange mechanism mediated by OH bridges, and a interlayer antiferromagnetic (AF) coupling between the layers mediated by less intense dipolar interactions.[10] In contrast, in the case of α-Co(II) hydroxihalide phases, the presence of two coordination environments on metal ions (Co^{Oh} and Co^{Td}) results in new magnetic interactions. In addition to the already described F coupling between the Co^{Oh} and AF coupling between the layers, F coupling between the Co^{Td} and AF coupling between the Co^{Oh} with the Co^{Td} are also present.[11] The combinations of these couplings result in non compensated magnetic interactions leading to ferrimagnetic regions, and therefore, a very complex magnetic behaviour.[45] Indeed, the theoretical results reproduce this magnetic behaviour (see Table S3, Table S4, Figure S8 and Figure S9), suggesting a stronger dependence on Co^{Td} population over the influence of the nature of the halide (see Table S5).

The Figure S10 depicts the thermal variations of magnetic susceptibility by the temperature products (χ.T) for all the samples. The χ.T product remains nearly constant upon cooling down until *ca.* 50 K, followed by a sharp increase reaching a broad maximum value strongly depends on the halide (see Table 2). The inverse of the magnetic susceptibility (χ^{-1}) can be fitted according to a CurieWeiss law in the high temperature region (200-300 K). The Curie-Weiss temperature (θ_{CW}) and the constant C can be obtained from the fitting (Figure S10-inset) and are compiled in Table 2. As Co^{Td} amount decreases, the θ_{CW} change from negative value (AF behaviour) for α-F, to positive values (F behaviour) for the others family members, increasing their absolute value as increase the halide's size. On the other hand, dynamic AC susceptibility measurements with an external applied field of 3.95 Oe oscillating at different frequencies allow to confirm the spontaneous magnetization at low temperatures (T<30 K). The strong frequency dependence observed in the dynamic susceptibility suggest a spin glass-like behaviour which could be attributed to the presence of different sublattices or microdomains (see Figure S11).[45] Hysteresis loops were also recorded at 2 K confirming the presence of spontaneous magnetization at low temperatures for all the samples (see Figure S12). Different saturation values were obtained. The difference between the experimental value and the M_{sat} estimated employing a Néel model[45] can be attributed to the complex magnetic structure of these kind of compounds. Moreover, the differences are bigger as X become smaller (higher amount of Co^{Td}) due to an increase of uncompensated interactions (see SI, Figure S9 and Table S3), with a strong dependence of the coercive field. Nielson *et al.*[45] reported the magnetic susceptibility measurements to reveal uncompensated magnetization, for a family of α-Co(II) hydroxi chloride, in which the magnetic properties changed with the variation of Co^{Td} in the range $0.20 - 0.40$. They observed $\theta_{CW} > 0$ for $Co^{Td} = 0.20$ meanwhile the observed $\theta_{CW} < 0$ for $Co^{Td} > 0.30$. Moreover, employing the same synthetic approach, Du *et al.*[39] obtained $\theta_{CW} < 0$ for a α-Co(II) hydroxi bromide sample with $Co^{Td} = 0.35$. Furthermore, plotting the data C and θ_{CW} according the equation 1,

$$\frac{C}{\chi \mid \theta_{CW} \mid} + sgn(\theta_{CW}) = \frac{T}{\theta_{CW}} \tag{1}$$

α-**X**	Co^{Td}	H_c (Oe)	T_N (K)	θ_{CW} (K)	C ($emu.mol^{-1}.Oe^{-1}$)
α-F	0.33	455	8.1	-8.8	2.88
α-Cl	0.26	1435	9.6-27.6	11.3	4.33
α-Br	0.14	1375	28.7	18.4	2.74
α-I	0.12	730	8.2-23	15.6	2.93

Table 2: Experimental values obtained from magnetic measurement for α-**X** phases. H_c: coercive magnetic field; T_N: Neél temperature; θ_{CW}: Curie-Weiss temperature; C: Curie-Weiss constant.

positive and negative deflections from the ideal θ_{CW} behaviour can be clearly seen, which are indicative of compensated and uncompensated interactions, respectively.[45] Indeed, only uncompensated interactions are observed for α-F, showing the highest Co^{Td} amount (> 0.3), indicative of dominant intralayer AF coupling interactions between distinct polyhedral. The present results are in concordance with the already mentioned. All of them suggesting that the main influence on the of magnetic behaviour can be related with the Co^{Td} population, which is reflected in the presence of a glassy behaviour with high magnetic disorder.

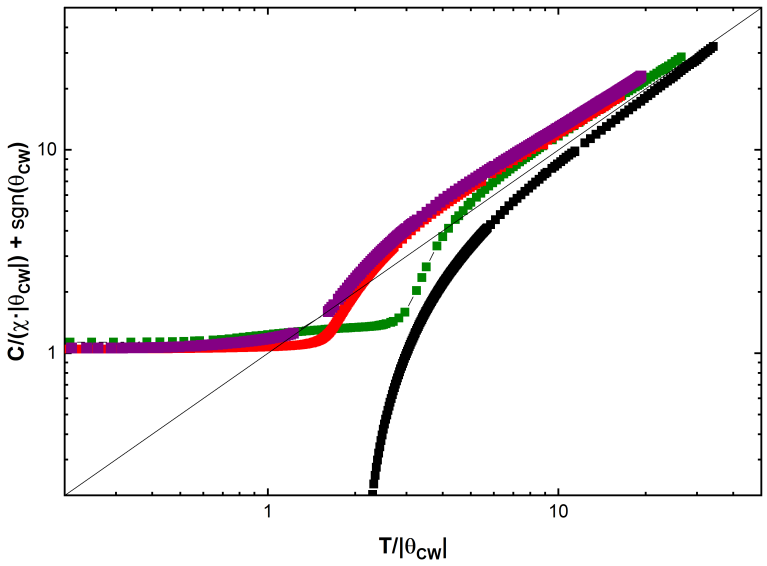

Figure 10: Temperature-dependent scaled inverse susceptibility for α-X phases: α-F (black), α-Cl (green), α-Br (red) and α-I (purple). Positive compensated and negative uncompensated deviations from ideal Curie-Weiss paramagnetism can be amplified.

Theoretical simulation can be also employed to understand the electronic properties of the α-**X** phases. The projected electronic density of states (PDOS) computed for the dehydrated layered Co(II) hydroxide halides are shown in Figure 11. It can be seen that the dominant contribution to the valence band around the Fermi level arises from the p states of X atoms, and that this contribution is larger as the anion's size increases due to the more efficient charge transfer. This effect produces the decrease of the band gap.

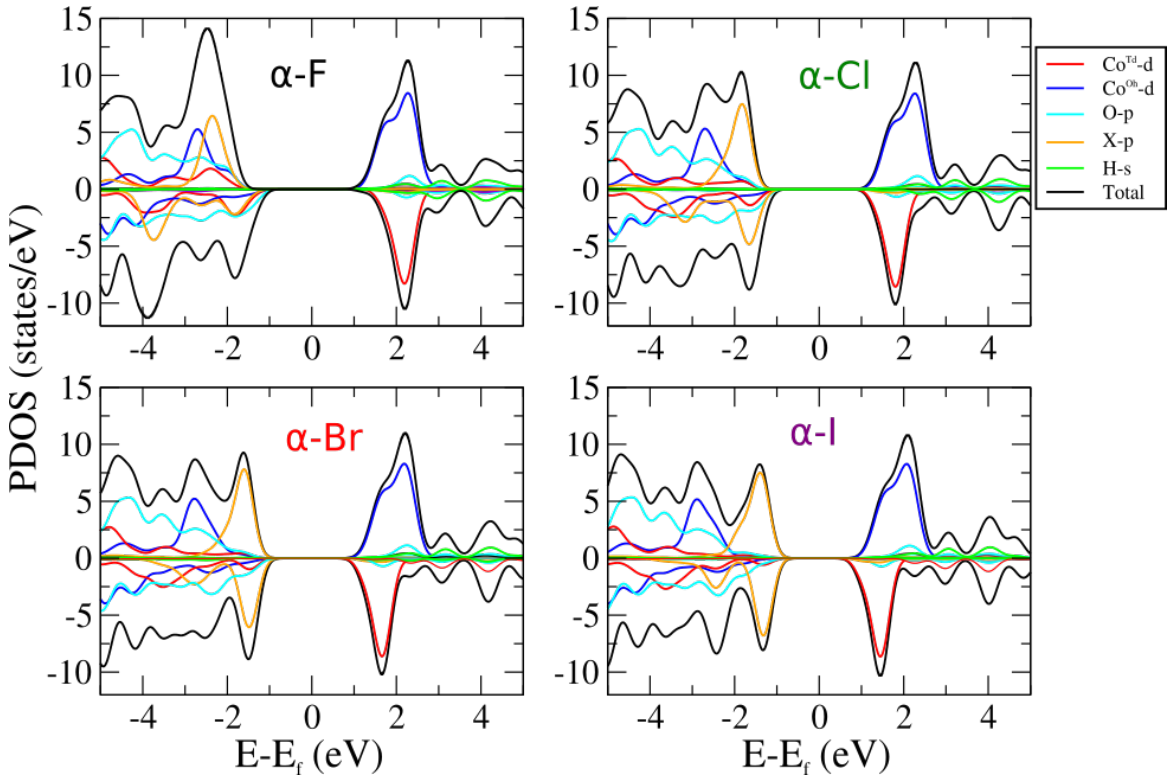

Figure 11: Projected density of states of the hydroxihalides (α-X), for supercells with $n = 3$, according to DFT+U. Near to the Fermi level, the major contribution to the electron density comes from the p orbitals of the halide atoms.

The dependence of E_{gap} with the fraction of Co^{Td} sites, is depicted for each halide in Figure 12; as the size of X increases, the electronic gap decreases regardless of the fraction of tetrahedral sites. Moreover, for each hydroxide halide, the E_{gap} increases with the rise of the Co^{Td} fraction. The electronic gap is extremely sensitive to composition and the nature of halide. In particular, this effect is more pronounced for the case of α-I, in which the E_{gap} is reduced from 1.35 to 0.6 eV. This change is attributable to the contribution of the d-states of the octahedral sites, that appear just above the gap (see Figure S13).

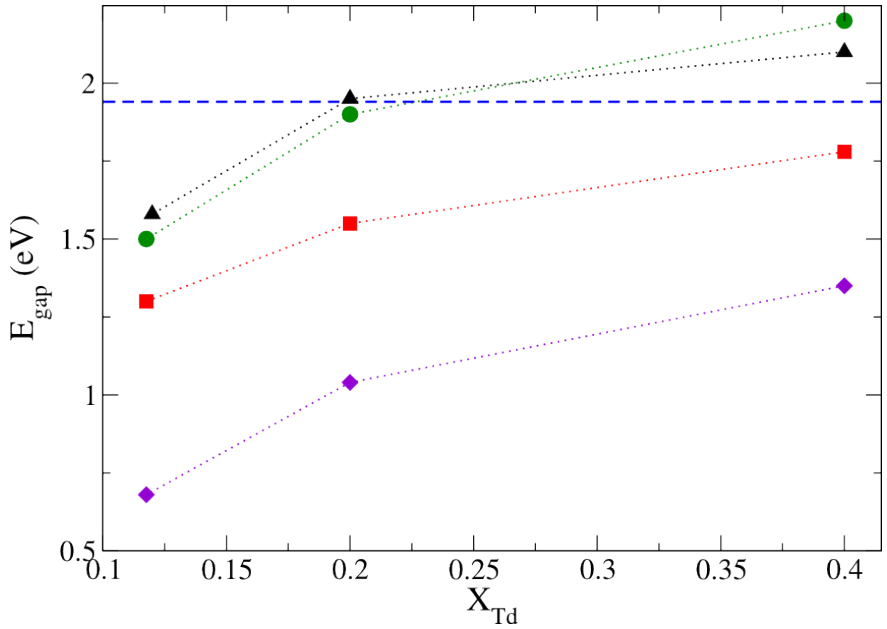

Figure 12: E_{gap} calculated with DFT+U, as a function of Co^{Td} cobalt molar fraction, X_{Td}, for a supercell of formula $Co_n^{Oh}Co_2^{Td}(OH)_{2n+2}X_2$ with X: F (black), Cl (green), Br (red) and I (purple). The E_{gap} calculated on similar basis for the β-$Co(OH)_2$, taken from Ref.[7], is represented by a blue dotted line.

Last but not least, the experimental conductivity properties have been studied on the α-X sample as a function of the temperatures using compressed pellet. The samples were dehydratated *in situ* at 127 °C (400 K) in order to ensure the comparison among the samples, avoiding any rehydration process during the samples processing.[46] Figure 13 depicts the electrical conductivity of the different samples, displaying higher conductivity values as the size of the halide increases. Remarkably, an Arrhenius fit of the data indicates a decrease in the thermal activation energies as the size of the halides increase (Figure 13-inset and Table S7), in good agrement with the theoretical calculation. It must be noticed, that even if the transport measurements match with the theoretical predictions, the difference in conductivity and activation energies cannot be directly related with a decrease in the E_{gap}, due to the different particle sizes, shapes and random orientations inherent to pellet preparation. Thus, further studies will be performed in the future on the basis of single flake measurements to properly compare the electrical E_{gap} of the different halides. These results highlight the inherent possibilities that these phases offer, since electronic and magnetic properties can be tailored by controlling the type of coordinated anion, and therefore, the fraction of tetrahedral sites. These results highlight the wide tunability of theses phases, since both electronic and magnetic properties can be tailored controlling the type of the coordinated anion as well as the Co^{Td} fraction.

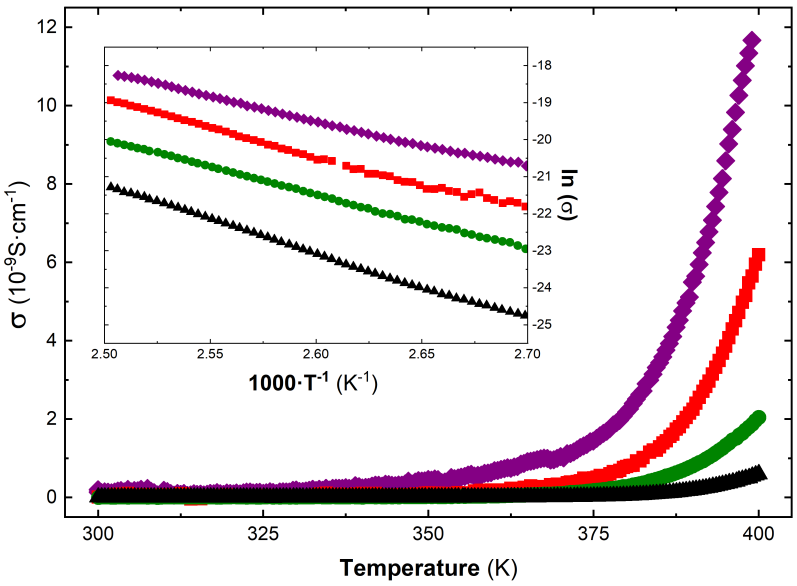

Figure 13: Conductivity (σ) as a function of temperature and Arrhenius plot of the logarithm of the conductance versus the inverse temperature (inset) of α-X phases: α-F (black), α-Cl (green), α-Br (red) and α-I (purple).

4 Conclusions

In this work we have synthesized for the first time at room-temperature and in a one-pot reaction, the complete family of highly crystalline Co(II) hydroxihalide employing the epoxide route. A thorough characterization including FESEM, EDS, UV-Vis diffuse reflectance, XPS, PXRD, TGA-MS, magnetic and conductivity measurements has been carried out, and these results were validated by DFT+U simulations. Experimental data supported by in silico results suggest that the magnetic behaviour strongly depends on Co^{Td} population, meanwhile the electrical properties are modulated by the type of halide atom, through a charge transfer mechanism. On the other hand, our synthetic approach shows a strong correlation between the Co^{Td} population with the size's of halide. To the best our knowledge, this is the first experimental and theoretical work on this sort of layers materials, paving the way towards a rational design of tunable electrical, optical and magnetic properties.

Supporting Information Available

alkalinization kinetic profiles, UV-Vis diffuse reflectance spectra, TGA analysis, macroscopic magnetic measurements, cell coordinate file, and electronic and magnetic properties section.

Acknowledgement

This work was supported by grants ANPCYT/PICT 2012 -2292 and UBACYT 20020160100124BA. We thank the allocation of computational time in the HPC Cluster CONICET-Rosario and CNEA. DH&VO acknowledge CONICET for postdoctoral scholarships, and R.T.-C., thanks the Ministerio de Ciencia, Innovación y Universidades for the F.P.I. predoctoral scholarships. G.A. acknowledges support by the European Union (ERC-2018-StG 804110-2D-PnictoChem), the Spanish MINECO (Structures of Excellence María de Maeztu MDM-2015-0538), and the Generalitat Valenciana (CIDEGENT/2018/001). VO is member of ALN. Authors want to acknowledge G. Agustí and J. M. Martínez for magnetic measurements; and to deeply thank Dr. Paula C. Angelomé for access to TGA-MS and UV-Vis reflectance facilities, and the inspiring moments.

References

(1) Auerbach, S.; Carrado, K.; Dutta, P., *Handbook of Layered Materials*; Marcel Dekker Inc., New York: 2004.

(2) Abellán, G.; Martí-Gastaldo, C.; Ribera, A.; Coronado, E. Hybrid Materials Based on Magnetic Layered Double Hydroxides: A Molecular Perspective. *Accounts of Chemical Research* **2015**, *48*, 1601–1611.

(3) Rogez, G.; Massobrio, C.; Rabu, P.; Drillon, M. Layered hydroxide hybrid nanostructures: a route to multifunctionality. *Chem. Soc. Rev.* **2011**, *40*, 1031–1058.

(4) Wang, Q.; OHare, D. Recent Advances in the Synthesis and Application of Layered Double Hydroxide (LDH) Nanosheets. *Chemical Reviews* **2012**, *112*, 4124–4155.

(5) Garbarino, G.; Núez-Regueiro, M.; Armand, M.; Lejay, P. Low temperature electric pulse induced resistance switching in $Na_{0.5}\delta CoO_2$. *Applied Physics Letters* **2008**, *93*, 152110.

(6) Oestreicher, V.; Jobbágy, M.; Regazzoni, A. E. Halide Exchange on Mg(II)-Al(III) Layered Double Hydroxides: Exploring Affinities and Electrostatic Predictive Models. *Langmuir* **2014**, *30*, 8408–8415.

(7) Costantino, U.; Vivani, R.; Bastianini, M.; Costantino, F.; Nocchetti, M. Ion exchange and intercalation properties of layered double hydroxides towards halide anions. *Dalton Trans.* **2014**, *43*, 11587–11596.

(8) Lee, K. K.; Chin, W. S.; Sow, C. H. Cobalt-based compounds and composites as electrode materials for high-performance electrochemical capacitors. *Journal of Materials Chemistry A* **2014**, *2*, 17212–17248.

(9) Arencibia, N.; Oestreicher, V.; Viva, F. A.; Jobbágy, M. Nanotextured alpha Ni(II)-Co(II) hydroxides as supercapacitive active phases. *RSC Adv.* **2017**, *7*, 5595–5600.

(10) Hunt, D.; Garbarino, G.; Rodriguez-Velamazan, J. A.; Ferrari, V.; Jobbágy, M.; Scherlis, D. A. The magnetic structure of β-cobalt hydroxide and the effect of spin-orientation. *Phys. Chem. Chem. Phys.* **2016**, *18*, 30407–30414.

(11) Hunt, D.; Jobbágy, M.; Scherlis, D. A. Interplay of Coordination Environment and Magnetic Behavior of Layered Co(II) Hydroxichlorides: A DFT+U Study. *Inorganic Chemistry* **2018**, *57*, 4989–4996.

(12) Kurmoo, M. Magnetic metal-organic frameworks. *Chem. Soc. Rev.* **2009**, *38*, 1353–1379.

(13) Zadrozny, J. M.; Liu, J.; Piro, N. A.; Chang, C. J.; Hill, S.; Long, J. R. Slow magnetic relaxation in a pseudotetrahedral cobalt(II) complex with easy-plane anisotropy. *Chem. Commun.* **2012**, *48*, 3927–3929.

(14) Mondal, A.; Durdevic, S.; Chamoreau, L.-M.; Journaux, Y.; Julve, M.; Lisnard, L.; Lescouzec, R. A cyanide and hydroxo-bridged nanocage: a new generation of coordination clusters. *Chem. Commun.* **2013**, *49*, 1181–1183.

(15) Schwenzer, B.; Roth, K. M.; Gomm, J. R.; Murr, M.; Morse, D. E. Kinetically controlled vapor-diffusion synthesis of novel nanostructured metal hydroxide and phosphate films using no organic reagents. *J. Mater. Chem.* **2006**, *16*, 401–407.

(16) Kurmoo, M.; Kumagai, H.; Hughes, S. M.; Kepert, C. J. Reversible Guest Exchange and Ferrimagnetism ($T_C = 60.5$ K) in a Porous Cobalt(II)Hydroxide Layer Structure Pillared with trans-1,4-Cyclohexanedicarboxylate. *Inorganic Chemistry* **2003**, *42*, 6709–6722.

(17) Kurmoo, M. Ferrimagnetism in dicarboxylate-bridged cobalt hydroxide layers. *J. Mater. Chem.* **1999**, *9*, 2595–2598.

(18) Du, Y.; OHare, D. Observation of Staging during Intercalation in Layered α-Cobalt Hydroxides: A Synthetic and Kinetic Study. *Inorganic Chemistry* **2008**, *47*, 11839–11846.

(19) Ma, R.; Liu, Z.; Takada, K.; Fukuda, K.; Ebina, Y.; Bando, Y.; Sasaki, T. Tetrahedral Co(II) Coordination in α-Type Cobalt Hydroxide: Rietveld Refinement and X-ray Absorption Spectroscopy. *Inorganic Chemistry* **2006**, *45*, 3964–3969.

(20) Hawthorne, F.; Sokolova, E. Simonkolleite, $Zn_5(OH)_8Cl_2(H_2O)$, a decorated interrupted-sheet structure of the form $[M\phi_2]_4$. *Canadian Mineralogist* **2002**, *40*, 939–946.

(21) Neilson, J. R.; Schwenzer, B.; Seshadri, R.; Morse, D. E. Kinetic Control of Intralayer Cobalt Coordination in Layered Hydroxides: $Co^{Oct}_{1-0.5x}Co^{tet}_x(OH)_2Cl_x.(H_2O)_n$. *Inorganic Chemistry* **2009**, *48*, 11017–11023.

(22) Liu, Z.; Ma, R.; Osada, M.; Takada, K.; Sasaki, T. Selective and Controlled Synthesis of α and β-Cobalt Hydroxides in Highly Developed Hexagonal Platelets. *Journal of the American Chemical Society* **2005**, *127*, 13869–13874.

(23) Oestreicher, V.; Jobbágy, M. One-Pot Synthesis of $Mg_2Al(OH)_6Cl$-$1.5H_2O$ Layered Double Hydroxides: The Epoxide Route. *Langmuir* **2013**, *29*, 12104–12109.

(24) Oestreicher, V.; Fábregas, I.; Jobbágy, M. One-Pot Epoxide-Driven Synthesis of $M_2Al(OH)_6Cl$-$1.5H_2O$ Layered Double Hydroxides: Precipitation Mechanism and Relative Stabilities. *The Journal of Physical Chemistry C* **2014**, *118*, 30274–30281.

(25) Tarutani, N.; Tokudome, Y.; Jobbágy, M.; Viva, F. A.; Soler-Illia, G. J.A. A.; Takahashi, M. Single-Nanometer-Sized Low-Valence Metal Hydroxide Crystals: Synthesis via Epoxide-Mediated Alkalinization and Assembly toward Functional Mesoporous Materials. *Chemistry of Materials* **2016**, *28*, 5606–5610.

(26) Giannozzi, P. et al. QUANTUM ESPRESSO: a modular and open-source software project for quantum simulations of materials. *Journal of Physics: Condensed Matter* **2009**, *21*, 395502 (19pp).

(27) Perdew, J. P.; Burke, K.; Ernzerhof, M. Generalized Gradient Approximation Made Simple. *Phys. Rev. Lett.* **1997**, *78*, 1396–1396.

(28) Anisimov, V. I.; Zaanen, J.; Andersen, O. K. Band theory and Mott insulators: Hubbard U instead of Stoner I. *Phys. Rev. B* **1991**, *44*, 943–954.

(29) Wang, L.; Maxisch, T.; Ceder, G. Oxidation energies of transition metal oxides within the GGA + U framework. *Phys. Rev. B* **2006**, *73*, 195107.

(30) Dalverny, A.; Filhol, J.; Lemoigno, F.; Doublet, M. Interplay between Magnetic and Orbital Ordering in the Strongly Correlated Cobalt Oxide: A DFT+U Study. *The Journal of Physical Chemistry C* **2010**, *114*, 21750–21756.

(31) Chen, J.; Wu, X.; Selloni, A. Electronic structure and bonding properties of cobalt oxide in the spinel structure. *Phys. Rev. B* **2011**, *83*, 245204.

(32) Chen, J.; Selloni, A. First Principles Study of Cobalt (Hydr)oxides under Electrochemical Conditions. *The Journal of Physical Chemistry C* **2013**, *117*, 20002–20006.

(33) Grimme, S. Semiempirical GGA-type density functional constructed with a long-range dispersion correction. *Journal of Computational Chemistry* **2006**, *27*, 1787–1799.

(34) Barone, V.; Casarin, M.; Forrer, D.; Pavone, M.; Sambi, M.; Vittadini, A. Role and effective treatment of dispersive forces in materials: Polyethylene and graphite crystals as test cases. *Journal of Computational Chemistry* **2009**, *30*, 934–939.

(35) Corso, A. D.; Conte, A. M. Spin-orbit coupling with ultrasoft pseudopotentials: Application to Au and Pt. *Phys. Rev. B* **2005**, *71*, 115106.

(36) Neilson, J.; Kurzman, J.; Seshadri, R.; Morse, D. Cobalt Coordination and Clustering in α-$Co(OH)_2$ Revealed by Synchrotron X-ray Total Scattering. *Chem. Eur. J.* **2010**, *16*, 9998–10006.

(37) Swain, C. G.; Scott, C. B. Quantitative Correlation of Relative Rates. Comparison of Hydroxide Ion with Other Nucleophilic Reagents toward Alkyl Halides, Esters, Epoxides and Acyl Halides1. *Journal of the American Chemical Society* **1953**, *75*, 141–147.

(38) S. Jayashree, R.; Vishnu Kamath, P. Electrochemical synthesis of α-cobalt hydroxide. *J. Mater. Chem.* **1999**, *9*, 961–963.

(39) Du, Y.; OHare, D. Synthesis of layered hydroxides using controlled ammonia vapor diffusion. *Journal of Physics and Chemistry of Solids* **2008**, *69*, 14th International Symposium on Intercalation Compounds, 1040 –1043.

(40) Hu, Z.-A.; Xie, Y.-L.; Wang, Y.-X.; Xie, L.-J.; Fu, G.-R.; Jin, X.-Q.; Zhang, Z.-Y.; Yang, Y.-Y.; Wu, H.-Y. Synthesis of α-Cobalt Hydroxides with Different Intercalated Anions and Effects of Intercalated Anions on Their Morphology, Basal Plane Spacing, and Capacitive Property. *The Journal of Physical Chemistry C* **2009**, *113*, 12502–12508.

(41) Choy, J.-H.; Kwon, Y.-M.; Han, K.-S.; Song, S.-W.; Chang, S. H. Intra- and inter-layer structures of layered hydroxy double salts, $Ni_{1x}Zn_{2x}(OH)_2(CH_3CO_2)_{2x}nH_2O$. *Materials Letters* **1998**, *34*, 356 –363.

(42) Iyi, N.; Fujii, K.; Okamoto, K.; Sasaki, T. Factors influencing the hydration of layered double hydroxides (LDHs) and the appearance of an intermediate second staging phase. *Applied Clay Science* **2007**, *35*, 218 –227.

(43) Jobbágy, M.; Iyi, N. Interplay of Charge Density and Relative Humidity on the Structure of Nitrate Layered Double Hydroxides. *The Journal of Physical Chemistry C* **2010**, *114*, 18153–18158.

(44) Chen, M.; Zhu, R.; Zhu, J.; He, H. Temperature-Dependent Structure and Dynamics of Water Intercalated in Layered Double Hydroxides with Different Hydration States. *The Journal of Physical Chemistry C* **2017**, *121*, 23752–23762.

(45) Neilson, J.; Morse, D.; Melot, B.; Shoemaker, D.; Kurzman, J.; Seshadri, R. Understanding complex magnetic order in disordered cobalt hydroxides through analysis of the local structure. *Phys. Rev. B* **2011**, *83*, 094418.

(46) Sun, P.; Ma, R.; Bai, X.; Wang, K.; Zhu, H.; Sasaki, T. Single-layer nanosheets with exceptionally high and anisotropic hydroxyl ion conductivity. *Science Advances* **2017**, *3*.

TOC Synopsis

Pure α-Co(II) hydroxihalides substituted with F, Cl, Br or I were prepared by a one-pot synthetic method based on the epoxide route at room temperature. A comprehensive physicochemical characterization (PXRD, XPS, TGA-MS, magnetic and conductivity measurements) is corroborated by DFT+U calculations. While the magnetic behaviour is strongly correlated with the Co^{Td} amount reflected in the presence of a glassy behaviour with high magnetic disorder, the electronic structure depends deeper on the nature of the halide.